Journal of Materials Chemistry A

Accepted Manuscript

ROYAL SOCIETY OF CHEMISTRY

www.rsc.org/materialsA

Stabilized Titanium Nitride Nanowires Supported Silicon Core-Shell Nanorods as High Capacity Lithium-Ion Anodes

*Hao Zheng, Shan Fang, Zhenkun Tong, Gang Pang, Laifa Shen, Hongsen Li, Liang Yang, and Xiaogang Zhang**

Received (in XXX, XXX) Xth XXXXXXXXX 20XX, Accepted Xth XXXXXXXXX 20XX
DOI: 10.1039/b000000x

In this work, TiN NWs supported silicon nanorods (TiN@Si NRs) are produced via direct radio frequency (RF) magnetron sputtering of Si deposition onto the surface of TiN NWs. Due to the superior mechanical stability and electrical conductivity of TiN, it provides more stable support and better conductive pathways for Si when compared with TiO_2. The unique core-shell TiN@Si NRs structure has enough void space to accommodate the large volume changes of Si during charge/discharge cycling. The novel 3D architecture electrode demonstrates exceptional electrochemical performances with ultrahigh specific capacity. Comparing with TiO_2@Si NRs, TiN@Si NRs electrode exhibits improved cycling performances, which can still retain a capacity of 3258.8 mAh g^{-1} after 200 cycles at 1 A g^{-1}. It should be noted that the TiN@Si NRs show an excellent rate performance even at a high current density (2256.6 mAh g^{-1} is realized at 10A g^{-1}). These results endow the electrodes with high power and long cycling stability.

Introduction

Rechargeable lithium-ion batteries (LIBs) are considered one of the most attractive technologies for a high power/energy density in power tools, vehicle electrification and portable devices. However, LIBs are still exposed to a large number of challenges in meeting the requirements of long cycle life, excellent rate capability, and high power density.[1-5] Currently, the commercial graphite anode with the limited theoretical capacity (372 mAh g^{-1}) need to be further improved.[6] For the past few years, many researchers have been committed themselves to develop high capacity anodes material such as silicon (Si), germanium (Ge) and tin (Sn) for high capacity LIBs.[7-9] Si is a promising alloy-type anode material due to its highest theoretical capacity (4200 mAh g^{-1}), which is 10 times higher than that of the current commercial graphite. However, Si usually suffers from huge volume change (300%) during lithium insertion/extraction process, contributing to a corresponding large capacity fade. This is ascribed to the pulverization of Si particles and loss of the electrical contact between the current collectors and Si. Besides, the electrical conductivity of Si is poor.[10-14] In order to improve the cycling stability, various Si-based anode nanostructures have been produced, including nanospheres, nanowires, nanotubes, yolk-shell structures, and single/multi layers thin films.[15-21] Amorphous Si-based thin films in particular have remarkable potential due to its smaller volume change and higher cycling stability.[22, 23] Up to now, diversified amorphous Si-based thin films have been prepared by magnetron sputtering, chemical vapor deposition (CVD), e-beam evaporation, vacuum evaporation, and pulsed laser deposition (PLD).[24-27] Simultaneously, the employed substrate such as three-dimensional (3D) structures can provide more contact area with the active materials and enough void space to accommodate the large volume changes of Si during cycling.[28, 29]

In our previous work, we have been successfully fabricated 3D titanium dioxide@germanium (TiO_2@Ge) core-shell nanorod arrays on carbon textiles.[30] The electrode exhibits the high reversible capacity, and outstanding rate capability, while the electrical conductivity of TiO_2 is unsatisfactory. In addition, TiO_2 may cause the irreversible capacity in the first lithiation process. It should be noted that the intrinsic electric conductivity of TiO_2 is poor, due to its large band gap energy (E_g=3.0 eV for rutile, E_g=3.2 eV for anatase). However, the band gap energy of TiN (E_g=2.0 eV) is smaller because the presence of N results in *p*-states above the valence band. So that titanium nitride (TiN) holds our promise because of its superior electrical conductivity ($\approx 10^5$ S m^{-1}, bulk), mechanical stability, chemical durability, and inactivity for Li-ion insertion/extraction in the range of 0.01-1.5 V.[31-33] For example, Tang *et al.* have synthesized TiN coated silicon nanoparticles with stable performance, excellent coulombic efficiency and enhanced rate performance.[34]

In this study, we demonstrate that stabilized titanium nitride nanowires (TiN NWs) on carbon textiles supported Si nanofilm, and further investigated as anode without using binder and conductive additives. First of all, the free-standing titanium dioxide nanowires (TiO_2 NWs) were grown on carbon textiles according to previous literature, then thermal treated in ammonia (NH_3) to obtain the TiN NWs. Stabilized TiN NWs supported Si core-shell nanorods (TiN@Si NRs) are produced by radio frequency (RF) magnetron sputtering of Si onto the surface of TiN NWs. The improved electrochemical performances of TiN@Si NRs can be attributed to the superior mechanical stability and electrical conductivity of TiN NWs. The unique 3D free-standing TiN@Si core-shell nanorods structure have enough void space to accommodate the large volume changes of Si during charge/discharge cycling as well as providing hierarchical pathways for electrolyte diffusion and effective ion transport.

Experiment Section

Preparation of TiN NWs on Carbon Textiles

The TiO_2 NWs were fabricated by a seed-assisted hydrothermal method according to the previous literature.[35] Briefly, carbon textiles (2*3 cm) were treated by nitric acid and reflux at 80 °C for 8 h, and then annealed in a muffle furnace for half an hour at 400 °C as the substrate for hydrothermal reaction. TiO_2 NWs were grown on carbon textiles by hydrolysis of titanium butoxide (TBOT) in a mixture solution of hydrochloric acid and acetone at

200 °C for 2 h. The TiO_2 NWs substrate was further thermal treatment in ammonia (NH_3) gas at 800 °C for 3 h to obtain the TiN NWs substrate.

Preparation of TiN@Si NRs and TiO_2@Si NRs

The TiN@Si NRs were prepared by direct RF magnetron sputtering in a JCP-650M6 system. Si nanofilms are deposited on TiN NWs substrate by magnetron sputtering of a high purity Si target (99.999%) with a diameter of 5 cm. The distance between the Si target and the substrate was controlled in about 8 cm, and a power of 80 W was carried out for the deposition with a constant time of 1 h. The TiO_2@Si NRs used TiO_2 NWs as substrates were fabricated according to the same sputtering process for TiN@Si NRs. In average, the mass of carbon textiles are 15.8 mg cm^{-2}, the mass of support framework TiO_2 is 3.0 mg cm^{-2}, the mass of support framework TiN is 2.3 mg cm^{-2}, the mass of Si coating is about 0.25 mg cm^{-2}, thus the weight percentage of Si is 7.7% for TiO_2@Si NRs and 9.8% for TiN@Si NRs. The specific capacity was calculated based on the active mass of Si for lithium-ion battery.

Characterization

The crystal structure and phase analysis were characterized by X-ray diffraction (XRD) (Bruker D8 advance) with Cu Kα radiation and Raman spectroscopy (LABRAM HR-800). Morphologies and microstructures of the samples were characterized by scanning electron microscopy (SEM, HITACHI S-4800), transmission electron microscopy (TEM, JEOL JEM-2100) and energy-dispersive X-ray spectroscopy (EDX). The samples were scratched from the films in absolute ethanol solution for TEM and EDX.

Electrochemical Test

The electrochemical performance measurements were tested by galvanostatic charge and discharge using the CR2016-type coin cell. The test electrodes were prepared by cutting the carbon textiles with a diameter of 1 cm and dried in a vacuum oven at 60 °C for 4 h. The cells were assembled with Lithium metal foil as the counter electrode in an argon-filled glove box. Polypropylene (PP) film was used as the separator. The electrolytes were used 1 M $LiPF_6$ in a mixture solution of ethylene carbonate (EC), and dimethyl carbonate (DMC) (1:1, by volume) contained 2% (V) fluoroethylene carbonate (FEC). Galvanostatic charge and discharge experiments were tested in the range of 0.01- 1.5 V (vs. Li/Li^+) using a CT2001A cell test instrument (LAND Electronic Co.). Cyclic voltammetry (CV) measurement was investigated on CHI 660C electrochemical workstation (Chenhua, China) between cutoff potential of 0.01-1.5 V (vs. Li/Li^+) at a scan rate of 0.1 mV s^{-1}. Electrochemical impedance spectroscopy (EIS) was measured in the frequency between 100 kHz and 0.01 Hz and the amplitude is 5 mV.

Results and Discussions

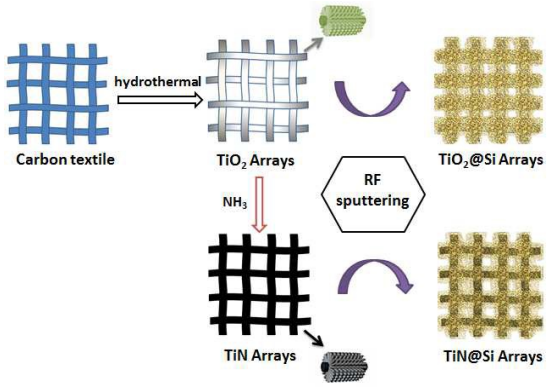

Fig. 1 Schematic diagram illustrate of the fabrication of TiN@Si NRs and TiO_2@Si NRs.

Fig. 1 illustrates the fabrication process of the free-standing TiN@Si NRs and TiO_2@Si NRs. TiO_2 NWs were first grown on the carbon textiles by a seed assisted hydrothermal approach and then further thermal treated in ammonia (NH_3) atmosphere to obtain the TiN NWs. Stabilized TiN NWs supported Si nanorods (TiN@Si NRs) are produced by direct radio frequency (RF) magnetron sputtering of Si onto TiN NWs substrate. TiO_2@Si NRs as a comparison sample are fabricated by the same method. Fig. S1 shows photographs of TiO_2 NWs, TiN NWs, TiO_2@Si NRs, and TiN@Si NRs. The obvious color change could be observed in the process of sample preparation and uniform color distribution of the NRs after sputtering indicates the uniform coating layer of Si supported on TiO_2 and TiN NWs.

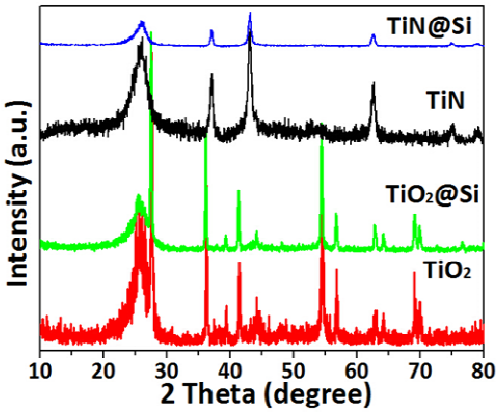

Fig. 2 XRD patterns of TiN@Si NRs (blue), TiN NWs (black), TiO_2@Si NRs (green), and TiO_2 NWs (red).

To characterize the crystalline structures of the nanowires and nanorods, XRD test is performed. XRD patterns of the TiN NWs and TiN@Si NRs were showed in Fig. 2. The major diffraction peaks of the annealed TiN NWs and TiN@Si NRs both can be indexed to crystal structure of cubic TiN (JCPDS no 65-5774). As a comparison, XRD patterns of the TiO_2 NWs and TiO_2@Si NRs were also shown in Fig. 2. The major diffraction peaks of the annealed TiO_2 NWs and TiO_2@Si NRs both are consistent with rutile phase of TiO_2 (JCPDS no 21-1276). Both of the nanorods samples present a similar XRD pattern with the initial nanowires substrate, but with lower diffracted intensities after RF magnetron sputtering. In addition, a weak peak located at around

26.2° is detected for all four samples, which can be attributed to disordered carbon derived from carbon textiles. Characteristic peak of crystalline Si at 28° is detected neither for the TiN@Si NRs nor TiO_2@Si NRs, which indicates that the sputtered Si is amorphous.[36, 37] It is reported that the amorphous Si is more durable to prevent volume expansion and provide more open structure for Li-ion transportation. Since the volume expansion of amorphous Si upon Li-ion insertion is homogeneous and causes less pulverization than that in the crystalline Si. In particular, the large inhomogeneous volume expansion for crystalline Si that occurs due to the different crystallographic orientation dependent lithiation in crystalline Si. [38, 39]

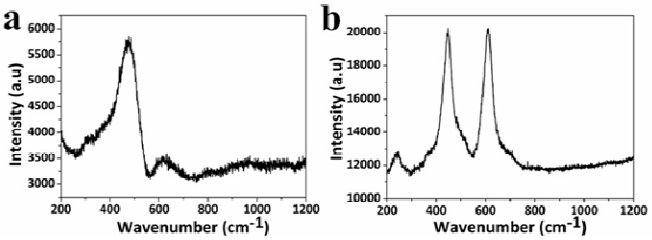

Fig. 3 Raman spectrums of TiN@Si NRs (a) and TiO_2@Si NRs (b).

Raman spectrum is used to further testify the real structure of Si. The Raman spectrum of TiN@Si NRs (Fig. 3a) shows a broad peak near 475 cm^{-1}, which is corresponding to the typical Si-Si bonds vibration. The peak presence at 475 cm^{-1} which characterizes an amorphous region and absence of the peak around 520 cm^{-1} corresponding to a crystalline region identify that the sputtered Si is amorphous according to Raman which is consistent with the XRD results. The peaks at 202 and 324 cm^{-1} indicative for TiN are detected. The band observed around 630 cm^{-1} corresponds to the 2LA (longitudinal acoustic) second order phonon Raman scattering and TO (transverse optic) + TA (transverse acoustic) overtone of amorphous Si vibration modes.[23, 40, 41] The Raman spectrum of TiO_2@Si NRs (Fig. 3b) exhibits the characteristic peaks of TiO_2 that centered at 236, 448 and 609 cm^{-1}. The characteristic peak of amorphous Si is covered by the strong adjacent twin peaks. In addition, no other obvious peaks are detected on both TiN@Si NRs and TiO_2@Si NRs therefore the sputtered Si for this study should be regarded as purely amorphous.

As mentioned in experimental procedure, TiN@Si NRs and TiO_2@Si NRs are fabricated by sputtering Si on TiN NWs and TiO_2 NWs, respectively. SEM images of TiN NWs and TiN@Si NRs are represented in Fig. 4. The compared samples of TiO_2 NWs and TiO_2@Si NRs are represented in Fig. S2. From Fig. S2a, we can see the whole surface status of carbon textiles. Almost all the carbon fibers are covered by TiO_2 NWs uniformity and each carbon fiber with TiO_2 NWs has a diameter of about 15 μm (Fig. S2b). After further thermal treated in NH_3 atmosphere, the TiN NWs is obtained, as shown in Fig. 4a and b. As it is obviously seen from Fig. 4a, TiN NWs still keep the same arrays structure with TiO_2 NWs. However, TiN NWs with smaller diameter have more void space than TiO_2 NWs, as shown in Fig.

Fig. 4 SEM images of TiN NWs (a, b), TiN@Si NRs (c, d), TEM image of TiN@Si NR and corresponding EDX elemental mapping (e).

4b inset. It is understood that more void space can more effectively accommodate the large volume change of Si during cycling. The length of TiN NWs around 4 μm and the diameter is about 100 nm (inset of Fig. 4b). The length of TiO_2 NWs around 3μm and the diameter is about 150 nm (inset of Fig. S2b). From

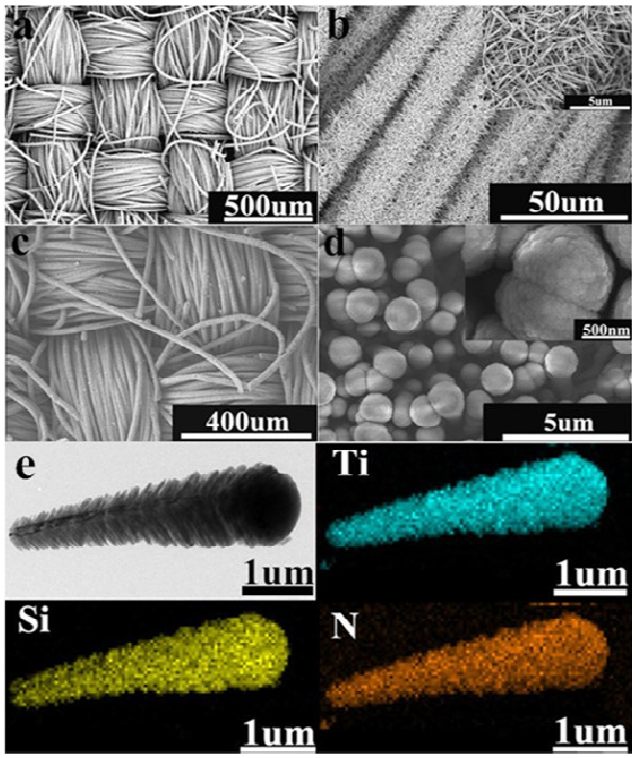

Fig. S2c and d, we can observe that the TiO_2@Si NRs still retained uniform arrays after sputtering. Each TiN@Si NR has a diameter about 500nm at the top as shown in inset of Fig. 4d. Each TiO_2@Si NR has a diameter in a range of 400 ~ 800 nm at the top as shown in inset of Fig. S2d. The SEM images of TiN@Si NRs are shown in Fig. 4c and d, which exhibit similar arrays to TiO_2@Si NRs. Besides, compared Fig. 4d with S2d inset, we can find that TiN@Si NRs still have more void space than that of TiO_2@Si NRs, which is benefit to accommodate the volume expansion. If we look closely in Fig. 4d inset, we can observe that the surfaces film of Si is consisted by ultrafine nanoparticles, which can provide more ion transportation paths and buffer the volume expansion. In addition, the unique feature of the nanorod attached on each carbon fiber will possess good electrical contact, resulting in better charge-transfer kinetics.

Transmission electron microscopy (TEM) is a more valid method to understand the morphologies and microstructures of the composite electrode. Fig. 4e shows the TEM image and the corresponding energy-dispersive X-ray spectroscopy (EDX) elemental mappings of single TiN@Si NR. It reveals that a single TiN NW is about 4 μm in length, which is consistent with the SEM image in Fig. 4b. The diameter of the nanorod is not the same from the top to the bottom because sputtering system has

the anisotropic deposition characteristics. From the homogeneous distribution of Silicon, Titanium and Nitrogen, we can see that Si is well coated on the surface of TiN NW. It can be concluded that we successfully fabricated the TiN@Si NRs with unique core-shell structure by direct RF magnetron sputtering technique. Fig. S2e shows the TEM image and the corresponding EDX elemental mappings of TiO_2@Si NRs. It can be clearly seen that the Si nanofilms are distributed uniformly on the surface of the TiO_2 NWs. The presence of Titanium and Oxygen are detected and the distributions of these elements also indicate that TiO_2 NWs are sure coated with the Si. The HRTEM images of the tail TiO_2@Si NR and TiN@Si NRs are shown in Fig. S3. The crystal TiO_2 and TiN coating by amorphous Si can be observed. The dimension of Si is about 15 ~ 20 nm in the bottom for both TiO_2@Si NRs and TiN@Si NRs.

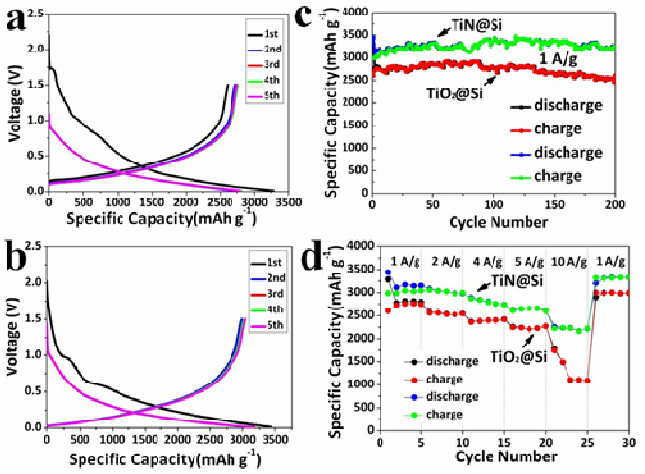

Fig. 5 Charge and discharge voltage profiles of TiO_2@Si NRs (a) and TiN@Si NRs (b) for 1st, 2nd, 3rd, 4th, 5th cycles tested between 0.01 and 1.5 V. (c) Cycling performances of TiO_2@Si NRs and TiN@Si NRs. (d) Rate performances of TiO_2@Si NRs and TiN@Si NRs.

The electrochemical performance of the composite electrode is evaluated by galvanostatic charge/discharge test at a current density of 1 A g^{-1} in the voltage ranges of 0.01-1.5 V *(vs. Li/Li$^+$)*. The 1st, 2nd, 3rd, 4th, and 5th cycle charge/discharge profiles of TiO_2@Si NRs have been shown in Fig. 5a. The initial charge/discharge capacities are 2603 and 3287.3 mAh g^{-1}, respectively, with a coulombic efficiency (CE) of 79.2%. And the voltage platform at 1.7-1.8 V could be ascribed to the lithiation of TiO_2 with Li-ion. Fig. 5b shows the 1st, 2nd, 3rd, 4th, and 5th cycle charge/discharge curves of TiN@Si NRs in the same test conditions. The initial charge/discharge capacities are 2986.4 and 3441.7 mAh g^{-1}, respectively, with a CE of 86.8%. The obvious voltage platform around 1.0 V is due to the formation of SEI. The two nanorods electrodes exhibit typical alloying charge/discharge curves corresponding to Si in the cycles, but the capacity of TiN@Si NRs is larger than TiO_2@Si NRs and TiN@Si NRs shows a higher initial CE. The different initial capacity of the two nanorods electrodes should attribute to the better electrical conductivity and inactivity for Li-ion insertion/extraction of TiN. The discharge capacities of TiN@Si NRs in the 2nd, 3rd, 4th, and 5th cycle are around 3109.9, 3175, 3148.1, 3155.7 mAh g^{-1}, respectively. And the discharge capacities of TiO_2@Si NRs in the 2nd, 3rd, 4th, and 5th cycle are around 2776, 2813.4, 2808.9, 2793.1 mAh g^{-1}, respectively. Cycling performances of TiO_2@Si NRs and TiN@Si NRs are tested for 200 cycles at a current density of 1 A g^{-1}, which is shown in Fig. 5c. After 200 charge/discharge cycles, the discharge capacity of TiO_2@Si NRs is 2460.4 mAh g^{-1} with a discharge capacity retention of 74.8% and a CE of 98.1%. However, TiN@Si NRs can still retain a capacity of 3258.8 mAh g^{-1} with a discharge capacity retention of 94.7% and a CE of 99.1% after 200 cycles. The capacity fading rate of TiO_2@Si NRs and TiN@Si NRs is around 0.09% and 0.03%/cycle over 200 cycles, respectively. The voltage-capacity profiles of TiO_2 NWs and TiN NWs on carbon textiles are shown in Fig. S4. We can see the capacity of TiO_2 NWs is 153 mAh g^{-1} and the TiN NWs with 122 mAh g^{-1} in the first cycle, so the capacity of TiO_2 NWs and TiN NWs are negligible compared with the Si anodes (4200 mAh g^{-1}). Both TiN@Si NRs and TiO_2@Si NRs show larger specific capacity than commercial graphite and present the high coulomb efficiency at the current density of 1A g^{-1}, as shown in Fig. S5. The high and stable CE indicates excellent cycling performances for both TiN@Si NRs and TiO_2@Si NRs. However, it should be noted that TiN@Si NRs presents a remarkable improvement in specific capacity when compared with TiO_2@Si NRs. The rate-capabilities of TiO_2@Si NRs and TiN@Si NRs are compared in Fig. 5d. As the current density increased from 1 A g^{-1} for the initial five cycles to 2 A g^{-1} for the following five cycles, the capacity drops from 3287.3 mAh g^{-1} to 2577.1 mAh g^{-1} for TiO_2@Si NRs and from 3441.7 mAh g^{-1} to 3078.8 mAh g^{-1} for TiN@Si NRs, respectively. TiN@Si NRs display the specific discharge capacity of 3441.7, 3078.8, 2885.6, 2620.7, and 2256.6 mAh g^{-1} at current densities of 1, 2, 4, 5, and 10 A g^{-1}, respectively. TiN@Si NRs obviously enhance the rate performance especially at a large current density of 10 A g^{-1}. This may be attributed to better electrical conductivity of TiN than TiO_2, which can guarantee the charge transport quickly. When the current density returned to 1 A g^{-1}, TiN@Si NRs can still have a high reversible capacity of 3204.3 mAh g^{-1}. The improved cycling performance and excellent rate-capability of TiN@Si NRs can be attributed to the unique TiN@Si core-shell nanorods structure, including that (1) superior electrical conductivity can guarantee the charge transport; (2) outstanding mechanical stability provides more stable support and better conductive pathways to Si; (3) the large open spaces between arrays can accommodate the large volume changes of Si during cycling and promote the absorption of the electrolyte; (4) TiN NWs directly stick on the surface of carbon fibers can decrease the interfacial charge transfer.

Fig. 6 CV curves of TiN@Si NRs (a) and TiO_2@Si NRs (b) in the potential range of 0.01-1.5 V at a scan rate of 0.1 mV s^{-1}.

To further research the electrochemical reactions and the insertion/extraction behaviors of Li-ion during charge/discharge process, cyclic voltammetry (CV) measurements are carried out in the potential range of 0.01-1.5 V (vs. Li/Li$^+$) at a scan rate of 0.1 mV s^{-1} for the first three cycles, as shown in Fig. 6. Fig. 6a shows CV curves of TiN@Si NRs, the cathodic peak locates at the potential of 0.7 V in the first cycle can be assigned to the formation of solid electrolyte interphase (SEI) film and the

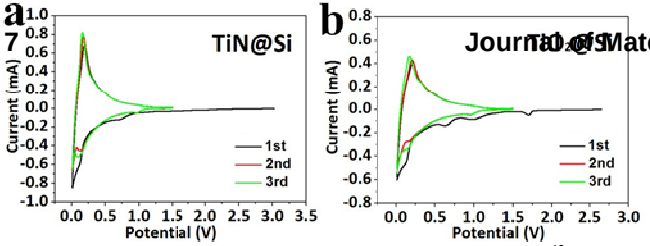

cathodic peak disappeared in the subsequent cycles.[42] Besides, the curve presents a small cathodic peak at 0.38 V and a sharp peak at 0.05 V, which is corresponded to the formation of Li-Si phase.[43] It should be noted that the cathodic peaks at around 1.0 V appear in the following two cycles, which can be attributed to the formation of SEI film.[44] Then, an anodic peak at around 0.2 V in the first cycle is related to the transformation from Li-Si phase to amorphous Si.[38] In addition, the peak currents of anodic peaks in the following two cycles are higher, which may be related to Li diffusion in the films.[43] A similar situation also appears in TiO_2@Si NRs, as shown in Fig. 6b. Besides, there is a very small cathodic peak at 1.75 V in the first cycle and disappeared in the subsequent cycles for TiO_2@Si NRs. This peak corresponds to Li-ion inserted into TiO_2, which is one of the reasons for irreversible capacity loss and reduces the CE.[45] In addition, there is a weak peak at around 1.05 V in the first cycle can be attributed to Li-ion inserted into TiO_2 and the cathodic peak still appears in the subsequent cycles.[16]

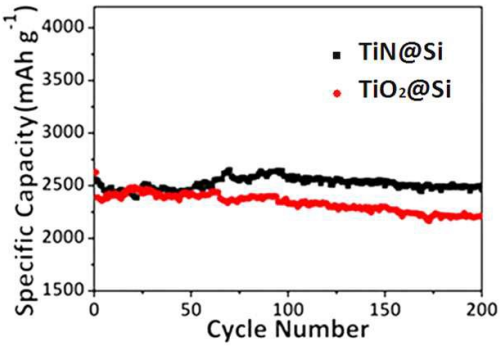

Fig. 7 Cycling performances of TiO_2@Si NRs and TiN@Si NRs at the high current density of 5A g^{-1}.

To research the cycling performances of TiN@Si NRs and TiO_2@Si NRs under high current density, both of the samples are characterized by charge/discharge cycling performances test under a current density of 5 A g^{-1} with cut-off voltages from 0.01 to 1.5 V (vs. Li/Li^+) at room temperature, as shown in Fig. 7. The initial discharge capacity of TiN@Si NRs and TiO_2@Si NRs are 2556.9 and 2626.6 mAh g^{-1}, respectively. After 200 cycles, the discharge capacity of TiN@Si NRs and TiO_2@Si NRs are 2465.3 mAh g^{-1} with a discharge capacity retention of 96.4% and 2211 mAh g^{-1} with a discharge capacity retention of 84.2%, respectively. It is quite clear that both TiN@Si NRs and TiO_2@Si NRs display considerable capacity at a high current density and TiN@Si NRs exhibit an excellent electrochemical performance. The typical SEM images of TiN@Si NRs and TiO_2@Si NRs after 20 cycles at 5 A g^{-1} with cut-off voltages from 0.01 to 1.5 V are shown in Fig. S6. From Fig. S6a and b, we can see that after 20 cycles 5 A g^{-1}, TiN@Si NRs still keep the original arrays architectures and even have void space, which is a direct proof of the structural integrity and stability of the materials. Although TiO_2@Si NRs also keep arrays structures, there is no void space can be observed from Fig. S6c and d. The TEM images of TiN@Si NRs and TiO_2@Si NRs after 20 cycles at 5 A g^{-1} are shown in Fig. S7. We can see the good electrode contact could still keep after cycles. In order to investigate the outstanding electrochemical performance of TiN@Si NRs, the electronic conductivity admeasurement for TiN@Si NRs and TiO_2@Si NRs are carried out. The electronic conductivity admeasurement is realized by the four-point probe method. The electronic conductivity of TiN@Si NRs reaches up to 23.81 S cm^{-1} while the TiO_2@Si NRs is only 6.3 S cm^{-1}. Although the electronic conductivity of both composite electrodes mainly comes from the contribution of carbon textiles, we can see that TiN has better electronic conductivity than that of TiO_2. It goes without saying that excellent electronic conductivity could ensure good electronic transmission during charge/discharge cycles.

Conclusions

In conclusion, the 3D TiN@Si and TiO_2@Si core-shell nanorods electrodes have been successfully prepared by a controllable RF magnetron sputtering method. These composite electrode exhibits high capacity and good rate performance as an anode materials for Li-ion battery. TiN@Si NRs electrode shows much better electrochemical performance than TiO_2@Si NRs. TiN@Si NRs can still retain a specific capacity of 3258.8 mAh g^{-1} at a current density of 1 A g^{-1} after 200 cycles. It should be noted that the TiN@Si NRs exhibits excellent rate capacity of 2256.6 mAh g^{-1} at a high current density of 10A g^{-1}. It indicates that the free-standing core-shell nanorods arrays structure may a promising candidate for thin-film batteries or flexible solid-state Li-ion batteries. The approach for prepared TiN@Si NRs and TiO_2@Si NRs can be extended to improve the electrochemical performances of other electroactive materials for Li-ion batteries.

Acknowledgements

This work was supported by the National Basic Research Program of China (973 Program) (No. 2014CB239701), National Natural Science Foundation of China (No. 21173120, 51372116), Natural Science Foundation of Jiangsu Province (BK2011030), the Fundamental Research Funds for the Central Universities of NUAA (NP2014403), A Project Funded by the Priority Academic Program Development of Jiangsu Higher Education Institutions.

Notes and references

Jiangsu Key Laboratory of Materials and Technology for Energy Conversion, College of Material Science and Engineering, Nanjing University of Aeronautics and Astronautics, Nanjing, 210016, P.R. China
Corresponding author Tel: +86 025 52112902; Fax: +86 025 52112626.
E-mail address: azhangxg@nuaa.edu.cn

1. M. Armand and J. M. Tarascon, *Nature*, 2008, **451**, 652.
2. J. B. Goodenough, *Accounts. Chem. Res.*, 2012, **46**, 1053.
3. L. Hu, H. Wu, F. La Mantia, Y. Yang and Y. Cui, *ACS Nano*, 2010, **4**, 5843.
4. J. Y. Choi, D. J. Lee, Y. M. Lee, Y. G. Lee, K. M. Kim, J. K. Park and K. Y. Cho, *Adv. Funct. Mater.*, 2013, **23**, 2108.
5. T. Song, J. Xia, J. H. Lee, D. H. Lee, M. S. Kwon, J. M. Choi, J. Wu, S. K. Doo, H. Chang and W. I. Park, *Nano Lett.*, 2010, **10**, 1710.

6. Y. W. Cheng, C. K. Lin, Y. C. Chu, A. Abouimrane, Z. Chen, Y. Ren, C. P. Liu, Y. Tzeng and O. Auciello, *Adv. Mater.*, 2014, **26**, 3724.
7. T. Song, H. Cheng, H. Choi, J. H. Lee, H. Han, D. H. Lee, D. S. Yoo, M. S. Kwon, J. M. Choi and S. G. Doo, *ACS Nano*, 2011, **6**, 303.
8. K. H. Seng, M. H. Park, Z. P. Guo, H. K. Liu and J. Cho, *Angew. Chem. Int. Ed.*, 2012, **51**, 5657.
9. J. Hassoun, G. A. Elia, S. Panero and B. Scrosati, *J. Power Sources*, 2011, **196**, 7767.
10. X. Su, Q. Wu, J. Li, X. Xiao, A. Lott, W. Lu, B. W. Sheldon and J. Wu, *Adv. Energy Mater.*, 2014, **4**, 1.
11. W. J. Zhang, *J. Power Sources*, 2011, **196**, 13.
12. M. Ge, J. Rong, X. Fang and C. Zhou, *Nano Lett.*, 2012, **12**, 2318.
13. T. H. Hwang, Y. M. Lee, B. S. Kong, J. S. Seo and J. W. Choi, *Nano Lett.*, 2012, **12**, 802.
14. V. Etacheri, R. Marom, R. Elazari, G. Salitra and D. Aurbach, *Energy Environ. Sci.*, 2011, **4**, 3243.
15. T. Wada, T. Ichitsubo, K. Yubuta, H. Segawa, H. Yoshida and H. Kato, *Nano Lett.*, 2014, **14**, 4505.
16. S. Fang, L. Shen, G. Y. Xu, P. Nie, J. Wang, H. Dou and X. G. Zhang, *ACS Appl. Mater. Interfaces*, 2014, **6**, 6497.
17. H. Wu, G. Chan, J. W. Choi, Y. Yao, M. T. McDowell, S. W. Lee, A. Jackson, Y. Yang, L. Hu and Y. Cui, *Nat. Nanotechnol.*, 2012, **7**, 310.
18. N. Liu, H. Wu, M. T. McDowell, Y. Yao, C. Wang and Y. Cui, *Nano Lett.*, 2012, **12**, 3315.
19. C. Yu, X. Li, T. Ma, J. Rong, R. Zhang, J. Shaffer, Y. An, Q. Liu, B. Wei and H. Jiang, *Adv. Energy Mater.*, 2012, **2**, 68.
20. W. Li, R. Yang, X. Wang, T. Wang, J. Zheng and X. Li, *J. Power Sources*, 2013, **221**, 242.
21. J. Song, S. Chen, M. Zhou, T. Xu, D. Lv, M. L. Gordin, T. Long, M. Melnyk and D. Wang, *J. Mater. Chem. A,* 2014, **2**, 1257.
22. S. Pal, S. S. Damle, S. H. Patel, M. K. Datta, P. N. Kumta and S. Maiti, *J. Power Sources*, 2014, **246**, 149.
23. V. Baranchugov, E. Markevich, E. Pollak, G. Salitra and D. Aurbach, *Electrochem. Commun.*, 2007, **9**, 796.
24. Y. Tang, X. Xia, Y. Yu, S. Shi, J. Chen, Y. Zhang and J. Tu, *Electrochim. Acta*, 2013, **88**, 664.
25. J. L. Goldman, B. R. Long, A. A. Gewirth and R. G. Nuzzo, *Adv. Funct. Mater.*, 2011, **21**, 2412.
26. P. R. Abel, A. M. Chockla, Y. M. Lin, V. C. Holmberg, J. T. Harris, B. A. Korgel, A. Heller and C. B. Mullins, *ACS Nano*, 2013, **7**, 2249.
27. M. T. McDowell and Y. Cui, *Adv. Energy Mater.*, 2011, **1**, 894.
28. Y. Zhang, X. Xia, X. Wang, Y. Mai, S. Shi, Y. Tang, C. Gu and J. Tu, *J. Power Sources*, 2012, **213**, 106.
29. X. Chen, K. Gerasopoulos, J. Guo, A. Brown, C. Wang, R. Ghodssi and J. N. Culver, *Adv. Funct. Mater.*, 2011, **21**, 380.
30. S. Fang, L. Shen, P. Nie,G. Y. Xu, L. Yang, H. Zheng and X. G. Zhang, *Part. Part. Syst. Char.*, 2014, **32**, 364.
31. Y. Qiu, K. Yan, S. Yang, L. Jin, H. Deng and W. Li, *ACS Nano*, 2010, **4**, 6515.
32. X. Lu, G. Wang, T. Zhai, M. Yu, S. Xie, Y. Ling, C. Liang, Y. Tong and Y. Li, *Nano Lett.*, 2012, **12**, 5376.
33. M. S. Balogun, M. Yu, C. Li, T. Zhai, Y. Liu, X. Lu and Y. Tong, *J. Mater. Chem. A*, 2014, **2**, 10825.
34. D. Tang, R. Yi, M. L. Gordin, M. Melnyk, F. Dai, S. Chen, J. Song and D. Wang, *J. Mater. Chem. A*, 2014, **2**, 10375.
35. G. Wang, H. Wang, Y. Ling, Y. Tang, X. Yang, R. C. Fitzmorris, C. Wang, J. Z. Zhang and Y. Li, *Nano Lett.*, 2011, **11**, 3026.
36. S. J. Lee, J. K. Lee, S. H. Chung, H. Y. Lee, S. M. Lee and H. K. Baik, *J. Power Sources*, 2001, **97**, 191.
37. L. F. Cui, L. Hu, J. W. Choi and Y. Cui, *ACS Nano*, 2010, **4**, 3671.
38. L. F. Cui, R. Ruffo, C. K. Chan, H. Peng and Y. Cui, *Nano Lett.*, 2008, **9**, 491.
39. B. Jerliu, E. Hüger, L. Dörrer, B. K. Seidlhofer, R. Steitz, V. Oberst, U. Geckle, M. Bruns and H. Schmidt, *J. Phys. Chem. C*, 2014, **118**, 9395.
40. F. Li, H. Yue, Z. Yang, X. Li, Y. Qin and D. He, *Mater. Lett.*, 2014, **128**, 132.
41. U. Tocoglu, O. Cevher, M. O. Guler and H. Akbulut, *Appl. Surf. Sci.*, 2014, **305**, 402.
42. X. Zhou, L. J. Wan and Y. G. Guo, *Small*, 2013, **9**, 2684.
43. W. Li, Y. Tang, W. Kang, Z. Zhang, X. Yang, Y. Zhu, W. Zhang and C. S. Lee, *Small*, 2014, **11**, 1345.
44. Y. Wen, Y. Zhu, A. Langrock, A. Manivannan, S. H. Ehrman and C. Wang, *Small*, 2013, **9**, 2810.
45. D. Wang, D. Choi, Z. Yang, V. V. Viswanathan, Z. Nie, C. Wang, Y. Song, J. G. Zhang and J. Liu, *Chem. Mater.*, 2008, **20**, 3435.

Stabilized Titanium Nitride Nanowires Supported Silicon Core-Shell Nanorods as High Capacity Lithium-Ion Anodes

Hao Zheng, Shan Fang, Zhenkun Tong, Gang Pang, Laifa Shen, Hongsen Li, Liang Yang, and Xiaogang Zhang*

The 3D TiN@Si and TiO_2@Si core-shell nanorods arrays electrodes have been successfully prepared by a controllable RF magnetron sputtering method. TiN@Si NRs electrode exhibits higher capacity and better rate performance than TiO_2@Si NRs. The improved electrochemical performances of TiN@Si NRs can be attributed to the superior mechanical stability and electrical conductivity of TiN NWs. The unique 3D free-standing TiN@Si core-shell nanorods structure have enough void space to accommodate the large volume changes of Si during charge/discharge cycling.